

Takeshi NAKANISHI and Tsuneya ANDO¹*Department of Applied Physics and DIMES, Delft University of Technology
Lorentzweg 1, 2628 CJ Delft, The Netherlands*¹*Institute for Solid State Physics, University of Tokyo
5-1-5 Kashiwanoha, Kashiwa, Chiba 277-8581*

The effective Hamiltonian for two crossed nanotubes is derived in a $\mathbf{k}\cdot\mathbf{p}$ scheme and the conductance between them is calculated in the Born approximation. The conductance is found to depend strongly on the crossing angle with large maxima at commensurate stacking of lattices of two nanotubes. In a magnetic field perpendicular to both nanotubes, these two maxima exhibit a field dependence completely different to each other.

§1. Introduction

Carbon nanotubes (CNs) are novel quantum wires consisting of rolled graphite sheets.¹⁾ Single-wall CNs can be synthesized in structures ~ 1 nm in diameter and microns long.^{2,3)} These molecules possess unique electronic properties due to their small diameter and variable lattice orientation. The purpose of this paper is to study electric transport through crossed single-wall CNs.

Recently, experimental studies of crossed CNs with electrical leads attached to each end of both nanotubes were reported.^{4,5)} In junctions of metallic CNs, surprisingly high conductances of $0.1 - 0.2e^2/h$ have been reported. Junctions of a metallic CN and a semiconducting CN behave as Schottky diodes.⁴⁾ The tunnel conductance of about $0.03e^2/h$ shows power-law behavior as a function of bias voltage and temperature,⁵⁾ which has been suggested to be described by a Tomonaga-Luttinger liquid model for tunneling.^{6,7)}

Transport properties of coupled CNs are interesting and theoretical studies have been reported. A deformation of crossed carbon nanotubes, which may affect the tunneling conductance between CNs, has been calculated by the use of molecular-dynamics simulations.^{4,8)} By means of a pseudopotential local-density-functional method a pseudogap has been predicted to appear for an orientationally ordered crystal of CNs due to intertube transfer.^{9,10)} An orientation dependence has also been found by taking into account the tunneling between propagating Bloch states on neighboring tubes.¹¹⁾ The pseudogap has also been found in a tight-binding calculation on a double-wall nanotube.¹²⁾

Many theoretical studies have clarified the electric transport properties of isolated single-wall CNs as has been reviewed in ref. 13. Effects of impurity scattering were studied in detail and the possibility of complete absence of back scattering was predicted except for scatterers having a potential range smaller than the lattice constant and proven rigorously.¹⁴⁾ This intriguing fact could be related to Berry's phase acquired by a rotation in the wave-vector space for a system described by

a $\mathbf{k}\cdot\mathbf{p}$ Hamiltonian which is same as Weyl's equation for a neutrino.¹⁵⁾ The conductance was also calculated in a tight-binding model as a function of the strength of the potential.^{16,17)} Effects of scattering by a short-range and huge defect potential were studied in the presence and absence of a magnetic field.¹⁸⁻²³⁾ The conductance is shown to be quantized into zero, one, and two times of the conductance quantum $e^2/\pi\hbar$ depending on the type of the vacancy. The conductance of a connection of different CNs with topological defects has been calculated in the presence and absence of the magnetic field and universal power-law dependence was found.²⁴⁻²⁷⁾ Effects of long-range Coulomb interactions were studied and explicit predictions were made on the temperature dependence of the conductivity and the tunnel conductance between CN and a metallic contact.^{6,7,28-30)}

In this paper, we shall study the conductance between crossed metallic CNs with arbitrary chirality. In §2 an effective-mass Hamiltonian is derived in the presence of interlayer transfer integrals between two graphite sheets. In §3, transmission probabilities are calculated explicitly for metallic CNs both in the presence and in the absence of a magnetic field in the Born approximation. The numerical results for simple models are shown in §4 and for a realistic model in §5. The conclusions are given in §6.

§2. Effective-Mass Equation

The structure of a two-dimensional (2D) graphite is shown in Fig. 1 together with the first Brillouin zone and coordinate systems to be used in the following. In 2D graphite, two bands having approximately a linear dispersion cross the Fermi level (chosen at $\varepsilon=0$) at K and K' points of the first Brillouin zone. The wave vectors of the K and K' points are given by $\mathbf{K}=(2\pi/a)(1/3, 1/\sqrt{3})$ and $\mathbf{K}'=(2\pi/a)(2/3, 0)$. For states in the vicinity of $\varepsilon=0$, the amplitude of the wave function at \mathbf{R}_i^A of site A and \mathbf{R}_i^B of site B, where the subscript $i=1$ or 2 numbering the graphite layer has been introduced, is written as

$$\begin{aligned}\psi_{Ai}(\mathbf{R}_i^A) &= \exp(i\mathbf{K}\cdot\mathbf{R}_i^A)F_{Ai}^K(\mathbf{R}_i^A) + e^{i\eta_i} \exp(i\mathbf{K}'\cdot\mathbf{R}_i^A)F_{Ai}^{K'}(\mathbf{R}_i^A), \\ \psi_{Bi}(\mathbf{R}_i^B) &= -\omega e^{i\eta_i} \exp(i\mathbf{K}\cdot\mathbf{R}_i^B)F_{Bi}^K(\mathbf{R}_i^B) + \exp(i\mathbf{K}'\cdot\mathbf{R}_i^B)F_{Bi}^{K'}(\mathbf{R}_i^B),\end{aligned}\tag{2.1}$$

with $\omega = \exp(2\pi i/3)$, where η_i is the chiral angle between a chiral vector \mathbf{L}_i and the x_i' direction fixed on the

graphite plane and F_{Ai}^K , F_{Bi}^K , $F_{Ai}^{K'}$, and $F_{Bi}^{K'}$ are envelope functions assumed to be slowly-varying on the scale of the lattice constant a . We have $\mathbf{R}_i^A = n_a^i \mathbf{a} + n_b^i \mathbf{b} + \vec{\tau}$ and $\mathbf{R}_i^B = n_a^i \mathbf{a} + n_b^i \mathbf{b}$, where $\mathbf{a} = a(1, 0)$, $\mathbf{b} = a(-1/2, \sqrt{3}/2)$, $\vec{\tau} = \vec{\tau}_3 = a/2(1, -1\sqrt{3})$, and n_a^i and n_b^i are integers. We define $\vec{\tau}_1$ and $\vec{\tau}_2$ as shown in Fig. 1 (a), where $\vec{\tau}_1 = a(0, 1/\sqrt{3})$ and $\vec{\tau}_2 = a(-1/2, -1/2\sqrt{3})$. Further, the x_i axis is parallel to the chiral vector \mathbf{L}_i and y_i -axis is parallel to the axis of CN i , where CN2 is lying on top of the CN1 as shown in Fig. 1 (c).

In the nearest-neighbor tight-binding approximation, the equation of motion for the wave function on site A on the first graphite sheet is given by

$$\begin{aligned} \varepsilon \psi_{A1}(\mathbf{R}_1^A) = & -\gamma_0 \sum_{l=1}^3 \psi_{B1}(\mathbf{R}_1^A - \vec{\tau}_l) \\ & - \sum_{\mathbf{R}_2^A} t(\mathbf{R}_1^A, \mathbf{R}_2^A) \psi_{A2}(\mathbf{R}_2^A) - \sum_{\mathbf{R}_2^B} t(\mathbf{R}_1^A, \mathbf{R}_2^B) \psi_{B2}(\mathbf{R}_2^B), \end{aligned} \quad (2.2)$$

where γ_0 is a transfer integral between nearest-neighbor sites on the sheet, and $t(\mathbf{R}_1^A, \mathbf{R}_2^A)$ and $t(\mathbf{R}_1^A, \mathbf{R}_2^B)$ are interlayer transfer integrals. When we substitute eq. (2.1) into the above equation, we get

$$\begin{aligned} & \varepsilon (e^{i\mathbf{K} \cdot \mathbf{R}_1^A} F_{A1}^K(\mathbf{R}_1^A) + e^{i\eta_1} e^{i\mathbf{K}' \cdot \mathbf{R}_1^A} F_{A1}^{K'}(\mathbf{R}_1^A)) \\ = & e^{i\mathbf{K} \cdot \mathbf{R}_1^A} \gamma e^{i\eta_1} (\hat{k}_x' - i\hat{k}_y') F_{B1}^K(\mathbf{R}_1^A) + e^{i\mathbf{K}' \cdot \mathbf{R}_1^A} \gamma (\hat{k}_x' + i\hat{k}_y') F_{B1}^{K'}(\mathbf{R}_1^A) \\ & - \sum_{\mathbf{R}_2^A} t(\mathbf{R}_1^A, \mathbf{R}_2^A) [\exp(i\mathbf{K} \cdot \mathbf{R}_2^A) F_{A2}^K(\mathbf{R}_2^A) + e^{i\eta_2} \exp(i\mathbf{K}' \cdot \mathbf{R}_2^A) F_{A2}^{K'}(\mathbf{R}_2^A)] \\ & - \sum_{\mathbf{R}_2^B} t(\mathbf{R}_1^A, \mathbf{R}_2^B) [-\omega e^{i\eta_2} \exp(i\mathbf{K} \cdot \mathbf{R}_2^B) F_{B2}^K(\mathbf{R}_2^B) + \exp(i\mathbf{K}' \cdot \mathbf{R}_2^B) F_{B2}^{K'}(\mathbf{R}_2^B)], \end{aligned} \quad (2.3)$$

with $\gamma = (\sqrt{3}/2)a\gamma_0$ and $\hat{\mathbf{k}}' = -i\vec{\nabla}'$, where $F_{B1}^K(\mathbf{R}_1^A - \vec{\tau}_l)$ of the first term on the right-hand side has been expanded and the first order term has been retained.

In order to derive a Schrödinger equation for the envelopes at the K point, we first rewrite the above as

$$\begin{aligned} & \varepsilon [F_{A1}^K(\mathbf{R}_1^A) + e^{i\eta_1} e^{i(\mathbf{K}' - \mathbf{K}) \cdot \mathbf{R}_1^A} F_{A1}^{K'}(\mathbf{R}_1^A)] \\ = & \gamma e^{i\eta_1} (\hat{k}_x' - i\hat{k}_y') F_{B1}^K(\mathbf{R}_1^A) + e^{i(\mathbf{K}' - \mathbf{K}) \cdot \mathbf{R}_1^A} \gamma (\hat{k}_x' + i\hat{k}_y') F_{B1}^{K'}(\mathbf{R}_1^A) \\ & - \sum_{\mathbf{R}_2^A} t(\mathbf{R}_1^A, \mathbf{R}_2^A) [e^{i\mathbf{K} \cdot \mathbf{R}_2^A - i\mathbf{K} \cdot \mathbf{R}_1^A} F_{A2}^K(\mathbf{R}_2^A) + e^{i\eta_2} e^{i\mathbf{K}' \cdot \mathbf{R}_2^A - i\mathbf{K} \cdot \mathbf{R}_1^A} F_{A2}^{K'}(\mathbf{R}_2^A)] \\ & - \sum_{\mathbf{R}_2^B} t(\mathbf{R}_1^A, \mathbf{R}_2^B) [-\omega e^{i\eta_2} e^{i\mathbf{K} \cdot \mathbf{R}_2^B - i\mathbf{K} \cdot \mathbf{R}_1^A} F_{B2}^K(\mathbf{R}_2^B) + e^{i\mathbf{K}' \cdot \mathbf{R}_2^B - i\mathbf{K} \cdot \mathbf{R}_1^A} F_{B2}^{K'}(\mathbf{R}_2^B)]. \end{aligned} \quad (2.4)$$

We introduce a smoothing function $g(\mathbf{R})$ normalized in such a way that

$$\sum_{\mathbf{R}^A} g(\mathbf{R}^A) = \sum_{\mathbf{R}^B} g(\mathbf{R}^B) = 1. \quad (2.5)$$

We assume that $g(\mathbf{R})$ is real, has an appreciable amplitude in the region where $|\mathbf{R}|$ is smaller than a few times of the lattice constant, and decays rapidly with increasing $|\mathbf{R}|$. This means that spatial variation of envelope functions in this region can be safely neglected. Multiplying both sides of eq. (2.4) by $g(\mathbf{r}_1 - \mathbf{R}_1^A)$ and summing over \mathbf{R}_1^A , we arrive at

$$\begin{aligned} \varepsilon F_{A1}^K(\mathbf{r}_1) = & \gamma e^{i\eta_1} (\hat{k}_x' - i\hat{k}_y') F_{B1}^K(\mathbf{r}_1) \\ & - S^{-1} \int d\mathbf{r}_2 [t_{AA}^{KK}(\mathbf{r}_1, \mathbf{r}_2) F_{A2}^K(\mathbf{r}_2) + e^{i\eta_2} t_{AA}^{KK'}(\mathbf{r}_1, \mathbf{r}_2) F_{A2}^{K'}(\mathbf{r}_2) \\ & - \omega e^{i\eta_2} t_{AB}^{KK}(\mathbf{r}_1, \mathbf{r}_2) F_{B2}^K(\mathbf{r}_2) + t_{AB}^{KK'}(\mathbf{r}_1, \mathbf{r}_2) F_{B2}^{K'}(\mathbf{r}_2)], \end{aligned} \quad (2.6)$$

with

$$t_{S_1 S_2}^{K_1 K_2}(\mathbf{r}_1, \mathbf{r}_2) = \sum_{\mathbf{R}_1^{S_1}} \sum_{\mathbf{R}_2^{S_2}} g(\mathbf{r}_1 - \mathbf{R}_1^{S_1}) t(\mathbf{R}_1^{S_1}, \mathbf{R}_2^{S_2}) g(\mathbf{r}_2 - \mathbf{R}_2^{S_2}) e^{-i\mathbf{K}_1 \cdot \mathbf{R}_1^{S_1} + i\mathbf{K}_2 \cdot \mathbf{R}_2^{S_2}}, \quad (2.7)$$

where $S_1 = \{A, B\}$, $S_2 = \{A, B\}$, $\mathbf{K}_1 = \{\mathbf{K}, \mathbf{K}'\}$, $\mathbf{K}_2 = \{\mathbf{K}, \mathbf{K}'\}$, $S = \sqrt{3}a^2/2$ is the area of a unit cell, and use has been made of the relations such as

$$\begin{aligned} F_{A1}^K(\mathbf{r}_1) &= \sum_{\mathbf{R}_1^A} g(\mathbf{r}_1 - \mathbf{R}_1^A) F_{A1}^K(\mathbf{R}_1^A), \\ F_{B2}^K(\mathbf{r}_2) &= S^{-1} \int d\mathbf{r}_2 g(\mathbf{r}_2 - \mathbf{R}_2^B) F_{B2}^K(\mathbf{r}_2), \end{aligned} \quad (2.8)$$

which are valid for slowly-varying wave functions.

Similarly, the Schrödinger equation for the envelopes at the K' point is obtained as

$$\begin{aligned} \varepsilon F_{A1}^{K'}(\mathbf{r}_1) &= \gamma e^{-i\eta_1} (\hat{k}_x' + i\hat{k}_y') F_{B1}^{K'}(\mathbf{r}_1) \\ &- S^{-1} \int d\mathbf{r}_2 [e^{-i\eta_1} t_{AA}^{K'K}(\mathbf{r}_1, \mathbf{r}_2) F_{A2}^K(\mathbf{r}_2) + e^{i(\eta_2 - \eta_1)} t_{AA}^{K'K'}(\mathbf{r}_1, \mathbf{r}_2) F_{A2}^{K'}(\mathbf{r}_2) \\ &- \omega e^{i(\eta_2 - \eta_1)} t_{AB}^{K'K}(\mathbf{r}_1, \mathbf{r}_2) F_{B2}^K(\mathbf{r}_2) + e^{-i\eta_1} t_{AB}^{K'K'}(\mathbf{r}_1, \mathbf{r}_2) F_{B2}^{K'}(\mathbf{r}_2)]. \end{aligned} \quad (2.9)$$

Similar equations can be derived starting with a tight-binding equation of motion for a site B on CN1 and sites A and B on CN2. The results are summarized as

$$\begin{aligned} H_1 \mathbf{F}_1(\mathbf{r}_1) + S^{-1} \int d\mathbf{r}_2 H_{12}(\mathbf{r}_1, \mathbf{r}_2) \mathbf{F}_2(\mathbf{r}_2) &= \varepsilon \mathbf{F}_1(\mathbf{r}_1), \\ H_2 \mathbf{F}_2(\mathbf{r}_2) + S^{-1} \int d\mathbf{r}_1 H_{21}(\mathbf{r}_2, \mathbf{r}_1) \mathbf{F}_1(\mathbf{r}_1) &= \varepsilon \mathbf{F}_2(\mathbf{r}_2), \end{aligned} \quad (2.10)$$

with

$$H_i = \begin{pmatrix} 0 & \gamma(\hat{k}_{x_i} - i\hat{k}_{y_i}) & 0 & 0 \\ \gamma(\hat{k}_{x_i} + i\hat{k}_{y_i}) & 0 & 0 & 0 \\ 0 & 0 & 0 & \gamma(\hat{k}_{x_i} + i\hat{k}_{y_i}) \\ 0 & 0 & \gamma(\hat{k}_{x_i} - i\hat{k}_{y_i}) & 0 \end{pmatrix}, \quad (2.11)$$

$$\begin{aligned} H_{12}(\mathbf{r}_1, \mathbf{r}_2) &= H_{21}(\mathbf{r}_2, \mathbf{r}_1)^+ \\ &= \begin{pmatrix} -t_{AA}^{KK} & \omega e^{i\eta_2} t_{AB}^{KK} & -e^{i\eta_2} t_{AA}^{KK'} & -t_{AB}^{KK'} \\ \omega^{-1} e^{-i\eta_1} t_{BA}^{KK} & -e^{i(\eta_2 - \eta_1)} t_{BB}^{KK} & \omega^{-1} e^{i(\eta_2 - \eta_1)} t_{BA}^{KK'} & \omega^{-1} e^{-i\eta_1} t_{BB}^{KK'} \\ -e^{-i\eta_1} t_{AA}^{K'K} & \omega e^{i(\eta_2 - \eta_1)} t_{AB}^{K'K} & -e^{i(\eta_2 - \eta_1)} t_{AA}^{K'K'} & -e^{-i\eta_1} t_{AB}^{K'K'} \\ -t_{BA}^{K'K} & \omega e^{i\eta_2} t_{BB}^{K'K} & -e^{i\eta_2} t_{BA}^{K'K'} & -t_{BB}^{K'K'} \end{pmatrix}, \end{aligned} \quad (2.12)$$

and

$$\mathbf{F}_i(\mathbf{r}_i) = \begin{pmatrix} F_{Ai}^K(\mathbf{r}_i) \\ F_{Bi}^K(\mathbf{r}_i) \\ F_{Ai}^{K'}(\mathbf{r}_i) \\ F_{Bi}^{K'}(\mathbf{r}_i) \end{pmatrix}. \quad (2.13)$$

The effective couplings t_{AB} 's in $H_{12}(\mathbf{r}_1, \mathbf{r}_2)$ are given by eq. (2.7). In the above, the use has been made of the relations:

$$\hat{k}_{x_i} \pm i\hat{k}_{y_i} = e^{\mp i\eta_i} (\hat{k}_{x_i'} \pm i\hat{k}_{y_i'}). \quad (2.14)$$

In a magnetic field, we have to replace $\hat{\mathbf{k}}$ by $-i\vec{\nabla} + e\mathbf{A}/\hbar c$ with vector potential \mathbf{A} .^{31,32)}

When the contact area is sufficiently smaller than the surface of the CNs, we can safely replace the effective couplings by delta functions, because they have a range determined by $g(\mathbf{R})$ which is much shorter than the electron wavelength, i.e.,

$$t_{S_1 S_2}^{K_1 K_2}(\mathbf{r}_1, \mathbf{r}_2) = \delta(\mathbf{r}_1 - \mathbf{r}_1^0) \delta(\mathbf{r}_2 - \mathbf{r}_2^0) t_{S_1 S_2}^{K_1 K_2}, \quad (2.15)$$

where \mathbf{r}_1^0 and \mathbf{r}_2^0 are the contact position on each layer and

$$t_{S_1 S_2}^{K_1 K_2} = S^2 \sum_{\mathbf{R}_1^{S_1}} \sum_{\mathbf{R}_2^{S_2}} t(\mathbf{R}_1^{S_1}, \mathbf{R}_2^{S_2}) e^{-i\mathbf{K}_1 \cdot \mathbf{R}_1^{S_1} + i\mathbf{K}_2 \cdot \mathbf{R}_2^{S_2}}. \quad (2.16)$$

By using the relations $-\mathbf{K} \cdot \mathbf{R}^A = \mathbf{K}' \cdot \mathbf{R}^A - 2\pi/3$ and $-\mathbf{K} \cdot \mathbf{R}^B = \mathbf{K}' \cdot \mathbf{R}^B$, the following symmetry relations

hold:

$$\begin{aligned} t_{AA}^{KK} &= t_{AA}^{K'K'}^*, \quad t_{BB}^{KK} = t_{BB}^{K'K'}^*, \\ t_{AB}^{KK} &= t_{AB}^{K'K'}^* \omega^{-1}, \quad t_{BA}^{KK} = t_{BA}^{K'K'}^* \omega, \\ t_{AA}^{K'K'} &= t_{AA}^{KK}^*, \quad t_{BB}^{K'K'} = t_{BB}^{KK}^*, \\ t_{AB}^{K'K'} &= t_{AB}^{KK}^* \omega^{-1}, \quad t_{BA}^{K'K'} = t_{BA}^{KK}^* \omega. \end{aligned} \quad (2.17)$$

When the interlayer transfer integrals vary slowly as a function of a position in the range larger than the lattice constant, the coupling becomes much smaller and can be neglected because of the cancellation due to phase factors.

§3. Conductance

When the interlayer coupling is absent, the energy levels and wave functions are analytically obtained for $\varepsilon \sim 0$ by applying periodic boundary condition on each graphite sheet.³³⁾ We consider two metallic nanotubes with a same circumference L in the presence of a magnetic field H perpendicular to both axis directions as shown in Fig. 1 (c). When a magnetic field has components parallel to the axes, a band gap is induced by the corresponding flux due to an Aharonov-Bohm effect.³¹⁾ The electronic states for the gauge

$$\mathbf{A} = \left(0, \frac{LH}{2\pi} \sin \frac{2\pi x}{L}\right), \quad (3.1)$$

are³³⁾

$$\mathbf{F}_{sk}^K = \frac{1}{\sqrt{2A}} \begin{pmatrix} -is(k/|k|)F_-(x) \\ F_+(x) \\ 0 \\ 0 \end{pmatrix} \exp(iky), \quad (3.2)$$

and

$$\mathbf{F}_{sk}^{K'} = \frac{1}{\sqrt{2A}} \begin{pmatrix} 0 \\ 0 \\ +is(k/|k|)F_+(x) \\ F_-(x) \end{pmatrix} \exp(iky), \quad (3.3)$$

with

$$F_{\pm}(x) = \frac{1}{\sqrt{LI_0(\alpha)}} \exp\left[\pm \frac{1}{2}\alpha \cos \frac{2\pi x}{L}\right], \quad (3.4)$$

where A is the length of the nanotube, $s = +1$ and -1 for the conduction and valence band, respectively, α is the parameter proportional to the magnetic field defined as

$$\alpha = 2 \left(\frac{L}{2\pi l} \right)^2, \quad (3.5)$$

with $l = \sqrt{c\hbar/eH}$ being the magnetic length, and $I_0(z)$ is the modified Bessel function of the first kind defined as

$$I_0(z) = \int_0^\pi \frac{d\theta}{\pi} \exp(z \cos \theta). \quad (3.6)$$

The corresponding eigenenergies are given by $\varepsilon_s(k) = s\gamma|k|I_0(\alpha)^{-1}$, which gives the group velocity $v = (\gamma/\hbar)I_0(\alpha)^{-1}$ and density of states $D(0) = I_0(\alpha)/\pi\gamma$ at $\varepsilon = 0$. We should note that

$$I_0(z) \approx \begin{cases} 1 & (z \ll 1), \\ e^z/\sqrt{2\pi z} & (z \gg 1). \end{cases} \quad (3.7)$$

In high magnetic fields ($\alpha \gg 1$), $F_-(x)$ is localized around $x = \pm L/2$, $F_+(x)$ is localized around $x = 0$, the group velocity becomes exponentially small, and the density of states grows exponentially.

Low-energy states in the nanotubes are characterized by various length scales such as wavelength $2\pi/k$ in the axis direction, wavelength L in the circumference direction, and magnetic length l in strong magnetic fields. Below we shall restrict ourselves to a coupling with a range δ much smaller than these length scales, i.e., $\delta \ll 2\pi/k$, $\delta \ll L$, and $\delta \ll l$. In this case, the effective couplings are replaced by the delta potentials given by eq. (2.15) with eq. (2.16) and transmission is possible between regions around $\mathbf{r}_1^0 = 0$ on CN1 and $\mathbf{r}_2^0 = (\pm L/2, 0)$ on CN2.

Next, we calculate matrix elements $V_{1K_1\pm, 2K_2\pm}$ for electrons coming from the K_2 point in CN2 with positive (+) and negative (−) velocity and going to K_1 point in CN1 with positive (+) and negative (−) direction. Some

examples are given by

$$\begin{aligned} V_{1K\pm, 2K+} &= \frac{1}{2AL} \frac{1}{S} \left[\mp t_{AA}^{KK} F_+ F_- \pm i\omega e^{i\eta_2} t_{AB}^{KK} F_-^2 \right. \\ &\quad \left. - i\omega^{-1} e^{-i\eta_1} t_{BA}^{KK} F_+^2 - c t_{BB}^{KK} F_+ F_- \right], \\ V_{2K\pm, 1K+} &= \frac{1}{2AL} \frac{1}{S} \left[\mp t_{AA}^{KK*} F_+ F_- - i\omega^{-1} e^{-i\eta_2} t_{AB}^{KK*} F_-^2 \right. \\ &\quad \left. \pm i\omega e^{i\eta_1} t_{BA}^{KK*} F_+^2 - c^* t_{BB}^{KK*} F_+ F_- \right], \\ V_{1K'\pm, 2K'+} &= \frac{1}{2AL} \frac{1}{S} \left[\mp c t_{AA}^{K'K'} F_+ F_- \pm i e^{-i\eta_1} t_{AB}^{K'K'} F_+^2 \right. \\ &\quad \left. - i e^{i\eta_2} t_{BA}^{K'K'} F_-^2 - t_{BB}^{K'K'} F_+ F_- \right], \\ V_{2K'\pm, 1K'+} &= \frac{1}{2AL} \frac{1}{S} \left[\mp c^* t_{AA}^{K'K'*} F_+ F_- - i e^{i\eta_1} t_{AB}^{K'K'*} F_+^2 \right. \\ &\quad \left. \pm i e^{-i\eta_2} t_{BA}^{K'K'*} F_-^2 - t_{BB}^{K'K'*} F_+ F_- \right], \end{aligned} \quad (3.8)$$

with $c = \exp[i(\eta_2 - \eta_1)]$ and

$$F_{\pm} = \frac{1}{\sqrt{I_0(\alpha)}} \exp[\pm \alpha/2], \quad (3.9)$$

where use has been made of the symmetry of the effective couplings, eq. (2.17). Other elements are given in Appendix A.

In the absence of a magnetic field ($\alpha = 0$) we have $F_{\pm} = 1$ and in high magnetic fields ($\alpha \gg 1$) we have $F_+ \approx (2\pi\alpha)^{1/4}$ and $F_- \approx e^{-\alpha}(2\pi\alpha)^{1/4}$. In high magnetic fields, therefore, the terms including $F_+ F_- \propto e^{-\alpha} \sqrt{2\pi\alpha}$ or $F_-^2 \propto e^{-2\alpha} \sqrt{2\pi\alpha}$ decrease exponentially and the term with $F_+^2 \propto \sqrt{2\pi\alpha}$ remains. As shown in Appendix A, the term with F_+^2 is one containing $t_{BB}^{KK'}$, $t_{AA}^{K'K}$, $t_{BB}^{K'K*}$, and t_{AA}^{KK*} , in $V_{1K\pm, 2K'\pm}$, $V_{1K'\pm, 2K\pm}$, $V_{2K'\pm, 1K\pm}$, and $V_{2K\pm, 1K'\pm}$, respectively.

Conductances G_{ij} are defined as the sum of transmission probabilities between the j th and i th terminals as shown in Fig. 1 (c). In the Born approximation, these conductances are explicitly written for $\epsilon \sim 0$ as¹⁶⁾

$$\begin{aligned} G_{21} &= G_{34} = \frac{e^2}{\pi\hbar} \sum_{K_1, K_2} \left| \frac{A}{\hbar v} V_{2K_2-, 1K_1+} \right|^2, \\ G_{12} &= G_{43} = \frac{e^2}{\pi\hbar} \sum_{K_1, K_2} \left| \frac{A}{\hbar v} V_{1K_1-, 2K_2+} \right|^2, \\ G_{41} &= G_{32} = \frac{e^2}{\pi\hbar} \sum_{K_1, K_2} \left| \frac{A}{\hbar v} V_{2K_2+, 1K_1+} \right|^2, \\ G_{23} &= G_{14} = \frac{e^2}{\pi\hbar} \sum_{K_1, K_2} \left| \frac{A}{\hbar v} V_{2K_2-, 1K_1-} \right|^2. \end{aligned} \quad (3.10)$$

In the absence of a magnetic field we have $G_{21} = G_{12} = G_{43} = G_{34}$ and $G_{41} = G_{32} = G_{23} = G_{14}$, because of the time reversal symmetry. With the increase of a magnetic field, these four pairs of conductances are different in general.

§4. Simple Model

In order to understand qualitative features of effective couplings between two CNs, we shall consider CNs

with sufficiently large diameter and two commensurate stackings shown in Fig. 2. In Fig. 2 (a), a B site of CN2 is just above a B site of CN1 but A sites are not, just like the stacking in bulk graphite (Stack I). For this stacking, a coordinate transformation from (x'_2, y'_2) to (x'_1, y'_1) corresponds to an inversion around the x'_1 axis. As a result K and K' points in the (x'_2, y'_2) coordinate system are transformed to K and K' point with wave vector $\bar{\mathbf{K}} = (2\pi/a)(1/3, -1/\sqrt{3})$ and $\bar{\mathbf{K}}' = \mathbf{K}' = (2\pi/a)(2/3, 0)$, respectively, in the (x'_1, y'_1) coordinate system, as shown in Fig. 1 (b). In Fig. 2 (b), six-member rings are perfectly stacked on top of each other (Stack II). The coordinate transformation is an inverse around the y'_1 axis. Therefore, K points in the (x'_2, y'_2) coordinate system are transformed to K' points in the (x'_1, y'_1) system and vice versa. The transformed wave vectors are $\bar{\mathbf{K}} = (2\pi/a)(-2/3, 0)$ and $\bar{\mathbf{K}}' = (2\pi/a)(-1/3, 1/\sqrt{3})$.

We consider an effective transfer integral having a circular symmetry $t(\mathbf{R}_1, \mathbf{R}_2) = t(|\mathbf{R}_1 - \bar{\mathbf{R}}_2|)$ independent of A and B atoms, where $\bar{\mathbf{R}}_2$ denotes the point \mathbf{R}_2 expressed in the (x'_1, y'_1) coordinate system. Define

$$t_{S_1 S_2} = \sum_{\mathbf{R}_1^{S_1}} t(|\mathbf{R}_1^{S_1} - \bar{\mathbf{R}}_2^{S_2}|) e^{-i\mathbf{K}_1(\mathbf{R}_1^{S_1} - \bar{\mathbf{R}}_2^{S_2})}. \quad (4.1)$$

This can be regarded as an effective coupling of a single site $S_2 = \{A, B\}$ of CN2 with all $S_1 = \{A, B\}$ sites of CN1 and is independent of $\mathbf{K}_1 = \{K, K'\}$ and $\mathbf{R}_2^{S_2}$. In terms of $t_{S_1 S_2}$, we have

$$t_{S_1 S_2}^{K_1 K_2} = S^2 \sum_{\mathbf{R}_2^{S_2}} t_{S_1 S_2} e^{-i\mathbf{K}_1 \cdot \bar{\mathbf{R}}_2^{S_2} + i\mathbf{K}_2 \cdot \mathbf{R}_2^{S_2}}. \quad (4.2)$$

For the stack I, t_{BB} remains nonzero and $t_{AA} = t_{AB} = t_{BA} = 0$. For the stack II, on the other hand, $t_{AA} = t_{BB}$ remains nonzero and $t_{AB} = t_{BA} = 0$.

Figure 3 shows the calculated results of t_{BB} for both stackings as a function of the range for a Gaussian form $t(r) = t' \exp(-r^2/\delta'^2)$. When the range is sufficiently small ($\delta'/a \ll 1$), it stays close to t'_0 because the transfer integral does not vanish between atoms on top of each other. It starts to decrease due to cancellation of transfers among different atoms when $\delta'/a \sim 0.5$ and vanishes for $\delta'/a \gg 1$.

The above arguments are valid in general for the transfer integrals with a symmetry under 120° rotation. Further, the fact that the effective coupling becomes reduced considerably due to interferences of transfers between different atoms remains valid for more general cases of stackings of two CNs.

Equation (4.2) or eq. ? more generally shows that effective couplings for neighboring atoms can exhibit a complicated interference behavior when they are summed up. In order to see this behavior explicitly, we consider a simple model in which the transfer integral is t_0 only for atoms just on top of each other and lying in a disk with a given radius centered at a carbon B site in CN2. In this model, the coupling is given by eq. (4.2) with $t_{BB} = t_0$ and $t_{AA} = t_{AB} = t_{BA} = 0$ for the stack I and

with $t_{AA} = t_{BB} = t_0$ and $t_{AB} = t_{BA} = 0$ for the stack II. Further, we can rewrite eq. (4.2) as

$$t_{S_1 S_2}^{K_1 K_2} = S^2 \sum_{\mathbf{R}_2^{S_2}} t_{S_1 S_2} e^{-i(\mathbf{K}_1 - \bar{\mathbf{K}}_2) \cdot \bar{\mathbf{R}}_2^{S_2} - i\bar{\mathbf{K}}_2 \cdot \mathbf{O}_2}, \quad (4.3)$$

where \mathbf{O}_2 is the origin of the (x'_2, y'_2) coordinate system expressed in the (x'_1, y'_1) system.

For the stack I, we have $e^{i\bar{\mathbf{K}}_2 \cdot \bar{\mathbf{R}}_2} = e^{i\mathbf{K}_2 \cdot \bar{\mathbf{R}}_2}$. This shows that the phase factor disappears for the effective coupling between same points and therefore $t_{BB}^{KK} = t_{BB}^{K'K'} = N_B t_0 S^2$ where N_B is the total number of B sites contained in the disk. For the coupling between different points the phase factor is different for atoms contained in the disk, which lead to a cancellation (not complete) and a small value for $|t_{BB}^{KK'}| = |t_{BB}^{K'K}|$. For example, we have $t_{BB}^{KK'} = t_{BB}^{K'K*} = t_0 S^2$ for (i) of Fig. 2 (a) and $-2t_0 S^2$ for (ii), which does not increase in proportion to N_B but oscillates around zero.

For the stack II, on the other hand, a K point is converted into a K' point and a K' point into a K point when the coordinate is changed from (x'_2, y'_2) into (x'_1, y'_1) . Therefore, the phase factor disappears (or has a common value) for the effective coupling between K and K' points but does not for coupling between same K points or K' points. We have explicitly $t_{BB}^{KK'} = t_{BB}^{K'K} = N_B t_0 S^2$ and $t_{AA}^{KK} = t_{AA}^{K'K*} = N_A t_0 S^2 \omega$ with N_A being the number of connecting pairs of A sites. Because of the phase factors, $t_{AA}^{KK} = t_{AA}^{K'K'} = 0$ and $|t_{BB}^{KK}| = |t_{BB}^{K'K'}|$ remain small but nonzero. Figure 4 shows amplitudes of the effective couplings for the stack I and II as a function of the number N_B of connecting pairs of B sites. The diameter of the contact region is roughly given by $2\sqrt{SN_B/\pi}$ and is shown on the upper axis.

In the Born approximation, the conductances for the stack I at $\epsilon = 0$ are given by

$$\begin{aligned} G_{12} = G_{21} = G_{41} = G_{32} = G_{43} = G_{34} = G_{23} = G_{14} \\ = \frac{e^2}{\pi \hbar} \left(\frac{a}{L} \right)^2 \left(\frac{t_0}{\gamma_0} \right)^2 I_0(\alpha)^2 \\ \times \frac{1}{4} \left[2(N_B F_+ F_-)^2 + \left(\frac{|t_{BB}^{KK'}|}{S^2 t_0} \right)^2 (F_+^4 + F_-^4) \right], \end{aligned} \quad (4.4)$$

which are proportional to the squares of t_0/γ_0 and a/L . The first term in the bracket represents the contributions of $|t_{BB}^{KK}| = |t_{BB}^{K'K'}| = N_B t_0 S^2$ and the second term smaller $|t_{BB}^{KK'}| = |t_{BB}^{K'K}|$. This result is independent of chirality, i.e., the angle θ between CNs, and the phase of the effective couplings, corresponding to the fact that the effective coupling does not vanish only between B sites in eq. (3.8).

In the absence of a magnetic field, where $F_+ = F_- = 1$, the conductance is roughly proportional to N_B^2 when $N_B \gg 1$. With the increase of the magnetic field, however, the second term, giving only a small contribution in the absence of a magnetic field, increases and becomes dominant. Figure 5 shows calculated conductances for several values of N_B as a function of a magnetic field.

The corresponding $t_{BB}^{KK} = t_{BB}^{K'K'}$ and $t_{BB}^{KK'} = t_{BB}^{K'K}$ are shown in Fig. 4. Note that the result in the absence of a magnetic field is valid even in the case that the size of the coupling region is comparable to the circumference, because the amplitude of the wave function is independent of the position.

For the stack II the conductances are obtained by using eq. (3.8) as

$$\begin{aligned} G_{12} &= G_{43} = G_{21} = G_{34} \\ &= \frac{e^2}{\pi\hbar} \left(\frac{a}{L}\right)^2 \left(\frac{t_0}{\gamma_0}\right)^2 I_0(\alpha)^2 \frac{1}{4} \left[(N_A^2 + N_B^2)(F_+^4 + F_-^4) \right. \\ &\quad \left. - 4N_A N_B \cos\theta (F_+ F_-)^2 + 2 \left(\frac{|t_{BB}^{KK}| F_+ F_-}{S^2 t_0} \right)^2 \right], \end{aligned} \quad (4.5)$$

and

$$\begin{aligned} G_{32} &= G_{41} = G_{23} = G_{14} \\ &= \frac{e^2}{\pi\hbar} \left(\frac{a}{L}\right)^2 \left(\frac{t_0}{\gamma_0}\right)^2 I_0(\alpha)^2 \frac{1}{4} \left[(N_A^2 + N_B^2)(F_+^4 + F_-^4) \right. \\ &\quad \left. + 4N_A N_B \cos\theta (F_+ F_-)^2 + 2 \left(\frac{|t_{BB}^{KK}| F_+ F_-}{S^2 t_0} \right)^2 \right], \end{aligned} \quad (4.6)$$

with $\theta = \eta_1 + \eta_2$. The conductances depend on the angle θ but not on individual parameters η_1 and η_2 . The small effective intra-valley coupling $|t_{BB}^{KK}|$ gives a contribution to the conductance independent of θ . The difference between $G_{12} = G_{21}$ and $G_{32} = G_{41}$ lies in a cross term proportional to $N_A N_B \cos\theta$. A dominant contribution to the conductances comes from the first and second terms both in the absence and presence of a magnetic field when $N_B \gg 1$ and $N_A \gg 1$. The conductance increases exponentially with the field strength.

§5. Realistic Model

As a more realistic model we consider a transfer integral given by

$$\begin{aligned} t(\mathbf{R}_1, \mathbf{R}_2) &= \exp\left(-\frac{|d|}{\delta}\right) \left[t_\sigma \left(\frac{\mathbf{p}(\mathbf{R}_1) \cdot \mathbf{d}}{|d|} \right) \left(\frac{\mathbf{p}(\mathbf{R}_2) \cdot \mathbf{d}}{|d|} \right) \right. \\ &\quad \left. + t_\pi \{ (\mathbf{p}(\mathbf{R}_1) \cdot \mathbf{e})(\mathbf{p}(\mathbf{R}_2) \cdot \mathbf{e}) + (\mathbf{p}(\mathbf{R}_1) \cdot \mathbf{f})(\mathbf{p}(\mathbf{R}_2) \cdot \mathbf{f}) \} \right], \end{aligned} \quad (5.1)$$

where $\mathbf{d} = \tilde{\mathbf{R}}_2 - \tilde{\mathbf{R}}_1$ is the distance with three-dimensional coordinates $\tilde{\mathbf{R}}_1$ of an atom on CN1 and $\tilde{\mathbf{R}}_2$ of an atom on CN2, $\mathbf{p}(\mathbf{R}_1)$ and $-\mathbf{p}(\mathbf{R}_2)$ are unit vectors normal to CN at \mathbf{R}_1 and \mathbf{R}_2 , respectively, and $\mathbf{d}/|d|$, \mathbf{e} , and \mathbf{f} constitute a set of three orthogonal unit vectors.

A range of exponentials $\delta/a = 0.325$, and parameters $t_\sigma = 9.34\gamma_0$ and $t_\pi = -5.91\gamma_0$ are determined by requiring that eq. (5.1) reproduces the values $V_{pp}^\sigma = 4.37$ eV for the first term and $V_{pp}^\pi \sim -\gamma_0 = -2.77$ eV for the second term at the distance $a/\sqrt{3} = 1.42$ Å between nearest-neighbor atoms on a graphite sheet, and 0.39 eV for the first term at the interlayer distance of graphite $D_0 = 3.35$ Å.^{34–37)} The former two values are obtained by first-principles local-density functional calculations on polyacetylene.³⁸⁾ A Slater-Koster parameterization³⁴⁾ and these values

have been used in band structure calculations on thin CNs.³⁷⁾

In the following D_0 is assumed as the nearest-neighbor distance between crossed two CNs. In this case the transfer integral decays exponentially with the range of about $\delta' \sim 0.8a$ as a function of the distance on virtual two dimensional co-ordinate system. Calculated effective transfer integrals defined in eq. (4.1) for the stack I and II are $\sim 0.08\gamma_0$ for these parameters consistent with the result in a Gaussian model given in Fig. 3.

In explicit numerical calculations we consider armchair nanotubes CN1 and CN2, fix a B site of each CN on top of each other, and rotate CNs around the B site. Figure 6 shows the calculated amplitudes of the effective couplings as a function of the angle θ between armchair CNs with $L/\sqrt{3}a = 100$. Amplitudes $|t_{BB}^{KK}| = |t_{BB}^{K'K}|$ and $|t_{AA}^{KK}| = |t_{AA}^{K'K}|$ take a large peak $\sim 4.0 \times S^2 \gamma_0$ around $\theta = \pi/3$ and $|t_{BB}^{KK}| = |t_{BB}^{K'K}|$ around $\theta = 2\pi/3$ indicated by arrows. The stackings approximately correspond to the simple models of stack II and I, respectively, because the contact plains of two CNs are almost flat due to the large circumference.

By studying the dependence of

$$I(\mathbf{R}_2^{S_2}) = \sum_{\mathbf{R}_1^{S_1}} t(\mathbf{R}_1^{S_1}, \mathbf{R}_2^{S_2}) e^{i\mathbf{K}_2 \cdot \mathbf{R}_2^{S_2} - i\mathbf{K}_1 \cdot \mathbf{R}_1^{S_1}} \quad (5.2)$$

on $|\mathbf{R}_2^{S_2}|$, we can estimate the size of the contact region. Near $\theta = \pi/3$ and $2\pi/3$, $|I(0)| \sim 0.08\gamma_0$ and $|I(\mathbf{R})|$ decays almost exponentially with the range $\sim 3.9a$, which is a radius of the contact region. The half width of these peaks is about $0.12 \times \pi/3$, which corresponds to the condition that the ideal stacking is lost near this boundary of the contact region by the rotation.

The amplitudes of the effective couplings $|t_{AB}^{KK'}| = |t_{AB}^{K'K}|$ and $|t_{BA}^{KK'}| = |t_{BA}^{K'K}|$ have a dip at $\theta = \pi/3$, a small peak at both sides of the dip, and decreases with the increase of the distance from $\pi/3$. The amplitudes $|t_{AA}^{KK}| = |t_{AA}^{K'K}|$, $|t_{AB}^{KK}| = |t_{AB}^{K'K}|$, and $|t_{BA}^{KK}| = |t_{BA}^{K'K}|$ exhibit a similar behavior around $\theta = 2\pi/3$. These terms remain much smaller than those of the dominant amplitudes $|t_{BB}^{KK'}| = |t_{BB}^{K'K}|$ and $|t_{AA}^{KK'}| = |t_{AA}^{K'K}|$ near $\theta = \pi/3$ and $|t_{BB}^{KK}| = |t_{BB}^{K'K}|$ near $\theta = 2\pi/3$.

The presence of the dips corresponds to the complete absence of these terms for the stack I and II considered in the simple model. By rotation from the stack I and II, the transfer integrals lose the symmetry under the 120° rotation and the cancellation discussed for the simple model becomes incomplete. As a result the effective couplings increase by the rotation from $\pi/3$ and $2\pi/3$. Because of complicated interferences of various terms the effective amplitude exhibits a behavior different between the smaller and larger angle sides. The destructive superposition is almost perfect at $\theta = 1.12 \times \pi/3$ and $1.88 \times \pi/3$. Such a perfect cancellation seems to be present only for thick CNs $L/\sqrt{3}a \gtrsim 100$.

Figures 7 shows calculated conductances for several circumferences. For thick CNs ($L/\sqrt{3}a = 100$ and 50, in

particular), because dominant components of the effective couplings are much larger than small components, the conductances are mainly determined by the dominant elements and take a peak at $\theta = \pi/3$ and $\theta = 2\pi/3$. In fact, the conductances $G_{41} = G_{32}$ and $G_{12} = G_{21}$ have a peak with almost same height at $\theta = 2\pi/3$ corresponding to the stack I in the simple model (see eq. (4.4)). At $\theta = \pi/3$, on the other hand, the peak of $G_{41} = G_{32}$ is higher than that of $G_{12} = G_{21}$ due to the presence of a term proportional to $\cos \theta$ in eqs. (4.5) and (4.6). These peak heights are almost independent of the circumference, because the size of the effective contact region is proportional to the circumference and is cancelled by the factor $(a/L)^2$ in eqs. (4.4), (4.5), and (4.6).

With the decrease of the circumference L , the contact region becomes smaller and as a result the half width of the dominant couplings increases, leading to the increase in the width of the conductance peaks around $\theta = \pi/3$ and $2\pi/3$. In fact, the estimated radius of the effective contact area is $3.9a$, $2.6a$, $1.7a$, and $1.2a$ for $L/\sqrt{3}a = 100$, 50 , 20 , and 10 , respectively, which gives roughly the half width of peak $0.12\pi/3$, $0.18\pi/3$, $0.27\pi/3$, and $0.38\pi/3$, respectively. Further, the peak position for the dominant terms is shifted according to a change in the optimum condition of the effective couplings due to curvature effects and small terms having a dip at $\theta = \pi/3$ and $2\pi/3$ start to have an appreciable contribution to the conductance. As a result the conductance has a peak at a position away from $\theta = \pi/3$ and $2\pi/3$ and also a weaker θ dependence for thin CNs.

Figure 8 shows the calculated conductances in the presence of a magnetic field for $L/\sqrt{3}a = 100$. The conductance of the peak around $\theta = \pi/3$ corresponding to the stack II in the simple model increases exponentially with the magnetic field as shown in Fig. 8 (a). This is due to the fact that the dominant terms such as $t_{BB}^{KK'}$ and $t_{AA}^{K'K}$ shown in Fig. 6 mainly contribute to the conductance in both presence and absence of a field. On the other hand, the conductance at $\theta = 2\pi/3$ (stack I) changes its feature from a single-peak to a double-peak behavior with the increase of the field as shown in Fig. 8 (b). This is because the terms t_{BB}^{KK} and $t_{BB}^{K'K'}$ dominant in the absence of a field are replaced by terms like t_{BA}^{KK} and $t_{AB}^{K'K'}$ containing F_+^2 in eq. (3.8) in high magnetic fields.

Although not shown explicitly here, the peak conductance at $\theta = \pi/3$ reaches $\sim 0.82 \times e^2/\pi\hbar$ in the field $(l/2\pi L)^2 = 2$. In such a case, the lowest Born approximation starts to break down and multiple tunneling processes start to play important roles. Such higher order effects are left for a future study.

§6. Summary

We have derived an effective Hamiltonian describing coupling between two crossed carbon nanotubes in a $\mathbf{k}\cdot\mathbf{p}$ scheme and gave expressions of the conductances between them in a Born approximation. The results are summarized as follows.

The coupling is given by a sum of transfer integrals

between atoms in two nanotubes with phase factors oscillating in a $\sqrt{3} \times \sqrt{3}$ Kekule pattern corresponding to wave vectors of K and K' points. The effective coupling between an atom of one nanotube with all atoms of the other decreases rapidly due to cancellation when being summed up with the increase in the range of the transfer integral. It becomes vanishingly small when the range exceeds the lattice constant. In a realistic model, the effective range is comparable to the lattice constant and therefore the effective coupling is reduced considerably due to cancellation but remains still appreciable. For armchair nanotubes, dominant terms have a large peak at $\theta \approx \pi/3$ (stack II) and $2\pi/3$ (stack I) where the hexagons on both CNs stack in a commensurate way.

For thick nanotubes ($L/\sqrt{3}a \gtrsim 50$), the conductance between two armchair nanotubes exhibits a sharp peak at an angle corresponding to the stack I and II and remains vanishingly small in other cases. The conductance at the peaks is essentially independent of the nanotube diameter. With the decrease in the diameter, two peaks are broadened and their positions are slightly shifted due to curvature effects. For thin nanotubes ($L/\sqrt{3}a \sim 10$), the broadened peaks overlap each other and small terms giving only negligible effects in a thick nanotube contribute to the conductance. As a result, the conductance becomes nonzero for all angles but exhibits a large oscillation as a function of the angle.

When a magnetic field is applied perpendicular to the axis of both nanotubes, the conductance at the peak around stack I and II exhibits a behavior completely different from each other. The peak at $\theta = \pi/3$ (stack II) increases with the magnetic field. On the other hand, the peak at $\theta = 2\pi/3$ (stack I) is replaced by a double-peak behavior with a dip at $\theta = 2\pi/3$. These can be understood by the localization of the wave function at the top and bottom sides of nanotubes in magnetic fields. Because the density of states at Fermi energy increases exponentially, the lowest Born approximation becomes inappropriate and multiple tunneling processes become important in strong magnetic fields. This problem is left for a future study.

Acknowledgments

The authors wish to thank G. E. W. Bauer and Yu. N. Nazarov for helpful discussions. This work was supported in part by Grants-in-Aid for Scientific Research and for Priority Area, Fullerene Network, from Ministry of Education, Science and Culture and by NEDO. One of us (T.N.) acknowledges the support of JSPS Postdoctoral Fellowships for Research Abroad. Numerical calculations were performed in part on the FACOM VPP500 of the Supercomputer Center, Institute for Solid State Physics, University of Tokyo.

Appendix A: Matrix Elements

Matrix elements describing scattering between different nanotubes other than those shown in §3 are given

below:

$$\begin{aligned}
V_{1K\pm,2K'+} &= \frac{1}{2AL} \frac{1}{S} \left[\pm e^{i\eta_2} t_{AA}^{KK'} F_-^2 \mp i t_{AB}^{KK'} F_+ F_- \right. \\
&\quad \left. + i\omega^{-1} c t_{BA}^{KK'} F_+ F_- + \omega^{-1} e^{-i\eta_1} t_{BB}^{KK'} F_+^2 \right], \\
V_{1K'\pm,2K+} &= \frac{1}{2AL} \frac{1}{S} \left[\pm e^{-i\eta_1} t_{AA}^{K'K} F_+^2 \mp i\omega c t_{AB}^{K'K} F_+ F_- \right. \\
&\quad \left. + i t_{BA}^{K'K} F_+ F_- + \omega e^{i\eta_2} t_{BB}^{K'K} F_-^2 \right], \\
V_{2K'\pm,1K+} &= \frac{1}{2AL} \frac{1}{S} \left[\pm e^{-i\eta_2} t_{AA}^{KK'*} F_-^2 + i t_{AB}^{KK'*} F_+ F_- \right. \\
&\quad \left. \mp i\omega c^* t_{BA}^{KK'*} F_+ F_- + \omega e^{i\eta_1} t_{BB}^{KK'*} F_+^2 \right], \\
V_{2K\pm,1K'+} &= \frac{1}{2AL} \frac{1}{S} \left[\pm e^{i\eta_1} t_{AA}^{K'K*} F_+^2 + i\omega^{-1} c^* t_{AB}^{K'K*} F_+ F_- \right. \\
&\quad \left. \mp i t_{BA}^{K'K*} F_+ F_- + \omega^{-1} e^{-i\eta_2} t_{BB}^{K'K*} F_-^2 \right], \tag{A1}
\end{aligned}$$

$$\begin{aligned}
V_{1K\pm,2K-} &= \frac{1}{2AL} \frac{1}{S} \left[\pm t_{AA}^{KK} F_+ F_- \pm i\omega e^{i\eta_2} t_{AB}^{KK} F_-^2 \right. \\
&\quad \left. + i\omega^{-1} e^{-i\eta_1} t_{BA}^{KK} F_+^2 - c t_{BB}^{KK} F_+ F_- \right], \\
V_{2K\pm,1K-} &= \frac{1}{2AL} \frac{1}{S} \left[\pm t_{AA}^{KK*} F_+ F_- + i\omega^{-1} e^{-i\eta_2} t_{AB}^{KK*} F_-^2 \right. \\
&\quad \left. \pm i\omega e^{i\eta_1} t_{BA}^{KK*} F_+^2 - c^* t_{BB}^{KK*} F_+ F_- \right], \\
V_{1K'\pm,2K'-} &= \frac{1}{2AL} \frac{1}{S} \left[\pm c t_{AA}^{K'K'} F_+ F_- \pm i e^{-i\eta_1} t_{AB}^{K'K'} F_+^2 \right. \\
&\quad \left. + i e^{i\eta_2} t_{BA}^{K'K'} F_-^2 - t_{BB}^{K'K'} F_+ F_- \right], \\
V_{2K'\pm,1K'-} &= \frac{1}{2AL} \frac{1}{S} \left[\pm c^* t_{AA}^{K'K'*} F_+ F_- + i e^{i\eta_1} t_{AB}^{K'K'*} F_+^2 \right. \\
&\quad \left. \pm i e^{-i\eta_2} t_{BA}^{K'K'*} F_-^2 - t_{BB}^{K'K'*} F_+ F_- \right], \tag{A2}
\end{aligned}$$

and

$$\begin{aligned}
V_{1K\pm,2K'-} &= \frac{1}{2AL} \frac{1}{S} \left[\mp e^{i\eta_2} t_{AA}^{KK'} F_-^2 \mp i t_{AB}^{KK'} F_+ F_- \right. \\
&\quad \left. - i\omega^{-1} c t_{BA}^{KK'} F_+ F_- + \omega^{-1} e^{-i\eta_1} t_{BB}^{KK'} F_+^2 \right], \\
V_{1K'\pm,2K-} &= \frac{1}{2AL} \frac{1}{S} \left[\mp e^{-i\eta_1} t_{AA}^{K'K} F_+^2 \mp i\omega c t_{AB}^{K'K} F_+ F_- \right. \\
&\quad \left. - i t_{BA}^{K'K} F_+ F_- + \omega e^{i\eta_2} t_{BB}^{K'K} F_-^2 \right], \\
V_{2K'\pm,1K-} &= \frac{1}{2AL} \frac{1}{S} \left[\mp e^{-i\eta_2} t_{AA}^{KK'*} F_-^2 - i t_{AB}^{KK'*} F_+ F_- \right. \\
&\quad \left. \mp i\omega c^* t_{BA}^{KK'*} F_+ F_- + \omega e^{i\eta_1} t_{BB}^{KK'*} F_+^2 \right], \\
V_{2K\pm,1K'-} &= \frac{1}{2AL} \frac{1}{S} \left[\mp e^{i\eta_1} t_{AA}^{K'K*} F_+^2 - i\omega^{-1} c^* t_{AB}^{K'K*} F_+ F_- \right. \\
&\quad \left. \mp i t_{BA}^{K'K*} F_+ F_- + \omega^{-1} e^{-i\eta_2} t_{BB}^{K'K*} F_-^2 \right]. \tag{A3}
\end{aligned}$$

In the absence of a magnetic field, some of the above matrix elements become equal to each other because

$F_{\pm} = 1$. Explicitly, we have

$$\begin{aligned}
V_{1K+,2K+} &= c V_{2K'-,1K'-} \\
&= \frac{1}{2AL} \frac{1}{S} \left[-t_{AA}^{KK} + i\omega e^{i\eta_2} t_{AB}^{KK} - i\omega^{-1} e^{-i\eta_1} t_{BA}^{KK} - c t_{BB}^{KK} \right], \\
V_{1K'+,2K'+} &= c V_{2K-1K-} \\
&= \frac{1}{2AL} \frac{1}{S} \left[-c t_{AA}^{K'K'} + i e^{-i\eta_1} t_{AB}^{K'K'} - i e^{i\eta_2} t_{BA}^{K'K'} - t_{BB}^{K'K'} \right], \\
V_{1K+,2K'+} &= c V_{2K-1K'-} \\
&= \frac{1}{2AL} \frac{1}{S} \left[e^{i\eta_2} t_{AA}^{KK'} - i t_{AB}^{KK'} + i\omega^{-1} c t_{BA}^{KK'} + \omega^{-1} e^{-i\eta_1} t_{BB}^{KK'} \right], \\
V_{1K'+,2K+} &= c V_{2K'-1K-} \\
&= \frac{1}{2AL} \frac{1}{S} \left[e^{-i\eta_1} t_{AA}^{K'K} - i\omega c t_{AB}^{K'K} + i t_{BA}^{K'K} + \omega e^{i\eta_2} t_{BB}^{K'K} \right], \tag{A4}
\end{aligned}$$

and

$$\begin{aligned}
V_{1K-,2K+} &= c V_{2K'-,1K'+} \\
&= \frac{1}{2AL} \frac{1}{S} \left[t_{AA}^{KK} - i\omega e^{i\eta_2} t_{AB}^{KK} - i\omega^{-1} e^{-i\eta_1} t_{BA}^{KK} - c t_{BB}^{KK} \right], \\
V_{1K'-,2K'+} &= c V_{2K-,1K+} \\
&= \frac{1}{2AL} \frac{1}{S} \left[c t_{AA}^{K'K'} - i e^{-i\eta_1} t_{AB}^{K'K'} - i e^{i\eta_2} t_{BA}^{K'K'} - t_{BB}^{K'K'} \right], \\
V_{1K-,2K'+} &= c V_{2K-,1K'+} \\
&= \frac{1}{2AL} \frac{1}{S} \left[-e^{i\eta_2} t_{AA}^{KK'} + i t_{AB}^{KK'} + i\omega^{-1} c t_{BA}^{KK'} + \omega^{-1} e^{-i\eta_1} t_{BB}^{KK'} \right], \\
V_{1K'-,2K+} &= c V_{2K'-,1K+} \\
&= \frac{1}{2AL} \frac{1}{S} \left[-e^{-i\eta_1} t_{AA}^{K'K} + i\omega c t_{AB}^{K'K} + i t_{BA}^{K'K} + \omega e^{i\eta_2} t_{BB}^{K'K} \right]. \tag{A5}
\end{aligned}$$

References

- 1) S. Iijima: Nature **354** (1991) 56.
- 2) S. Iijima and T. Ichihashi: Nature **363** (1993) 603.
- 3) D. S. Bethune, C. H. Kiang, M. S. de Vries, G. Gorman, R. Savoy, J. Vazquez, and R. Beyers: Nature **363** (1993) 605.
- 4) M. S. Fuhrer, J. Nygard, L. Shih, M. Forero, Y.-G. Yoon, M. S. C. Mazzoni, H. J. Choi, J. Ihm, S. G. Louie, A. Zettl, and P. L. McEuen: Science **288** (2000) 494.
- 5) H. W. Ch. Postma, M. de Jonge, Z. Yao, and C. Dekker: Phys. Rev. B **62** (2000) R10653.
- 6) C. Kane, L. Balents, and M. P. A. Fisher: Phys. Rev. Lett. **79** (1997) 5086.
- 7) R. Egger and A. O. Gogolin: Phys. Rev. Lett. **79** (1997) 5082.
- 8) T. Hertel, R. E. Walkup, and P. Avouris: Phys. Rev. B **58** (1998) 13870.
- 9) P. Delaney, H. J. Choi, J. Ihm, S. G. Louie, and M. L. Cohen: Nature **391** (1998) 466.
- 10) Y.-K. Kwon, S. Saito, and D. Tománek: Phys. Rev. B **58** (1998) R13314.
- 11) A. A. Maarouf, C. L. Kane, and E. J. Mele: Phys. Rev. B **61** (2000) 11156.
- 12) Y.-K. Kwon and D. Tománek: Phys. Rev. B **58** (1998) R16001.
- 13) T. Ando: Semicond. Sci. & Technol. **15** (2000)

- R13.
- 14) T. Ando and T. Nakanishi: J. Phys. Soc. Jpn. **67** (1998) 1704. There are some typographical errors in this paper. For example, $u_A(\mathbf{R}_A)$ and $u_B(\mathbf{R}_B)$ appearing in the right hand side of eq. (2.18) should be replaced by $\tilde{u}_A(\mathbf{R}_A)$ and $\tilde{u}_B(\mathbf{R}_B)$, respectively.
 - 15) T. Ando, T. Nakanishi and R. Saito: J. Phys. Soc. Jpn. **67** (1998) 2857.
 - 16) T. Nakanishi and T. Ando: J. Phys. Soc. Jpn. **68** (1999) 561.
 - 17) T. Ando, T. Nakanishi and R. Saito: Microelectronic Engineering **47** (1999) 421.
 - 18) L. Chico, L. X. Benedict, S. G. Louie, and M. L. Cohen: Phys. Rev. B **54** (1996) 2600; Phys. Rev. B **61** (2000) 10511 (Erratum).
 - 19) M. Igami, T. Nakanishi and T. Ando: J. Phys. Soc. Jpn. **68** (1999) 716; Mol. Cryst. Liq. Cryst. **340** (2000) 719; Physica B **284-288** (2000) 1746; J. Phys. Soc. Jpn. **68** (1999) 3146.
 - 20) T. Ando, T. Nakanishi and M. Igami: J. Phys. Soc. Jpn. **68** (1999) 3994.
 - 21) H. J. Choi, J. Ihm, S. G. Louie, and M. L. Cohen: Phys. Rev. Lett. **84** (2000) 2917.
 - 22) T. Nakanishi, M. Igami and T. Ando: Physica E **6** (2000) 872.
 - 23) M. Igami, T. Nakanishi and T. Ando: J. Phys. Soc. Jpn. (submitted for publication).
 - 24) R. Saito, G. Dresselhaus and M. S. Dresselhaus: Phys. Rev. B **53** (1996) 2044.
 - 25) R. Tamura and M. Tsukada: Solid State Commun. **101** (1997) 601; Phys. Rev. B **55** (1997) 4991.
 - 26) T. Nakanishi and T. Ando: J. Phys. Soc. Jpn. **66** (1997) 2973; Physica B **249-251** (1998) 136.
 - 27) H. Matsumura and T. Ando: J. Phys. Soc. Jpn. **67** (1998) 3542.
 - 28) A. A. Odintsov, W. Smit, and H. Yoshioka: Europhys. Lett. **45** (1999) 598.
 - 29) H. Yoshioka and A. A. Odintsov: Synthetic Metals **103** (1999) 2527.
 - 30) H. Yoshioka: Phys. Rev. B **61** (2000) 7316.
 - 31) H. Ajiki and T. Ando: J. Phys. Soc. Jpn. **62** (1993) 1255.
 - 32) H. Ajiki and T. Ando: J. Phys. Soc. Jpn. **65** (1996) 505.
 - 33) T. Ando and T. Seri: J. Phys. Soc. Jpn. **66** (1997) 3558.
 - 34) J. C. Slater and G. F. Koster: Phys. Rev. **94** (1954) 1498.
 - 35) I. L. Spain: *Chemistry and Physics of Carbon*, Vol. 8, edited by P. L. Walker, Jr. and P. A. Thrower (Marcel Dekker, New York, 1973) p. 1.
 - 36) M. S. Dresselhaus, G. Dresselhaus, K. Sugihara, I. L. Spain, and, H. A. Goldberg: *Graphite Fibers and Filaments* (Springer-Verlag, Berlin, 1988), Vol. 5 of *Springer Series in Materials Science*.
 - 37) J. W. Mintmire and C. T. White: Carbon **33** (1995) 893.
 - 38) J. W. Mintmire and C. T. White: Phys. Rev. Lett. **50** (1983) 101; Phys. Rev. B **28** (1983) 3283.

Figure Captions

Fig. 1 (a) Lattice structure of a two-dimensional graph-

ite sheet. η_i is the chiral angle for CN1 ($i = 1$) and CN2 ($i = 2$). Two-dimensional co-ordinate systems (x'_1, y'_1) and (x'_2, y'_2) are introduced on each graphite sheet. The coordinates are chosen in such a way that x_i is along the circumference of a nanotube and y_i is along the axis for $i = 1$ and 2. (b) The first Brillouin zone and K and K' points. Reciprocal lattice vectors $\bar{\mathbf{a}}$ and $\bar{\mathbf{b}}$ are shown. (c) The coordinates for crossed nanotubes. θ is the angle between axes of CNs. A magnetic field H is applied in perpendicular to both CNs. Four terminals 1 and 3 of CN1, and 2 and 4 of CN2 are indicated.

Fig. 2 Lattice structure of a two-dimensional graphite sheet near the crossing of CNs for stack I (a) and stack II (b). Lower and upper CNs are shown by gray and black, respectively. A view from reverse is shown for upper CN, because (x_1, y_1) and (x_2, y_2) are chosen as shown in Fig. 1 (c). A and B sites are shown by the open and closed circles, respectively. For simple models with inter-layer transfer integral t_0 , examples of the contact region are indicated by the circles (i) and (ii).

Fig. 3 Effective transfer integrals t_{BB} for both stackings as the function of the range δ' . A Gaussian model is used in parallel graphite sheets.

Fig. 4 Absolute values of effective couplings as a function of the number N_B of B sites in the coupling region. $t_{BB}^{KK} = t_{BB}^{K'K'^*}$ for the stack I is equal to $t_{BB}^{KK'} = t_{BB}^{K'K'^*}$ for the stack II, which are shown by crosses. $t_{BB}^{KK'} = t_{BB}^{K'K'^*}$ for the stack II is also equal to $t_{BB}^{KK} = t_{BB}^{K'K'}$ for the stack II, which are shown by circles.

Fig. 5 Calculated conductance as a function of weak magnetic field for stack I. The magnetic field is perpendicular to both CNs as shown in Fig. 1 (c).

Fig. 6 Absolute values of effective couplings of the realistic model for $\eta_1 = \eta_2 = \pi/6$ (armchair CNs) and $L = 100\sqrt{3}a$ as a function of angle θ between CNs.

Fig. 7 Calculated conductances $G_{41} = G_{32} = G_{23} = G_{14}$ (a) and $G_{21} = G_{12} = G_{34} = G_{43}$ (b) between armchair CNs for several circumferences as a function of the angle θ in the absence of a magnetic field.

Fig. 8 Calculated conductance between armchair CNs for $L = 100\sqrt{3}a$ as a function of the angle θ for (a) $0.25\pi < \theta < 0.5\pi$ and (b) $0.5\pi < \theta < 0.75\pi$. Magnetic field is applied in perpendicular direction to the CNs. The origins of the conductances for several magnetic fields are shifted by 0.0005 in (b). Dot-dashed lines for $G_{23} = G_{14}$ almost overlap with solid lines for $G_{41} = G_{32}$. Note that, the conductances in (a) are one order of magnitude larger than in (b).

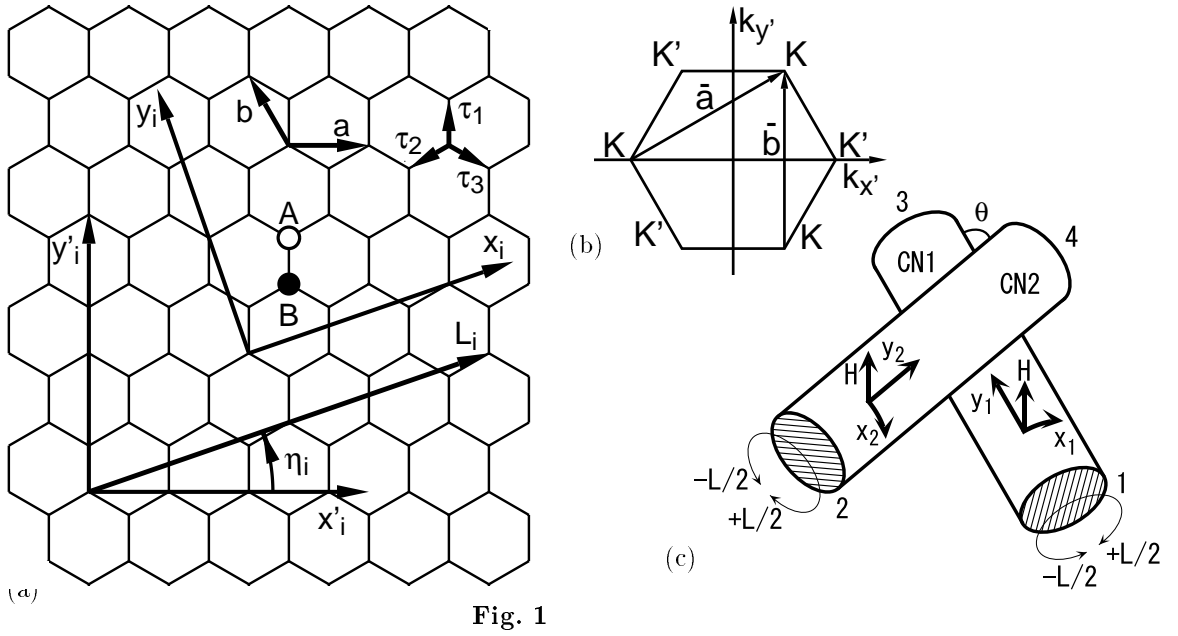


Fig. 1

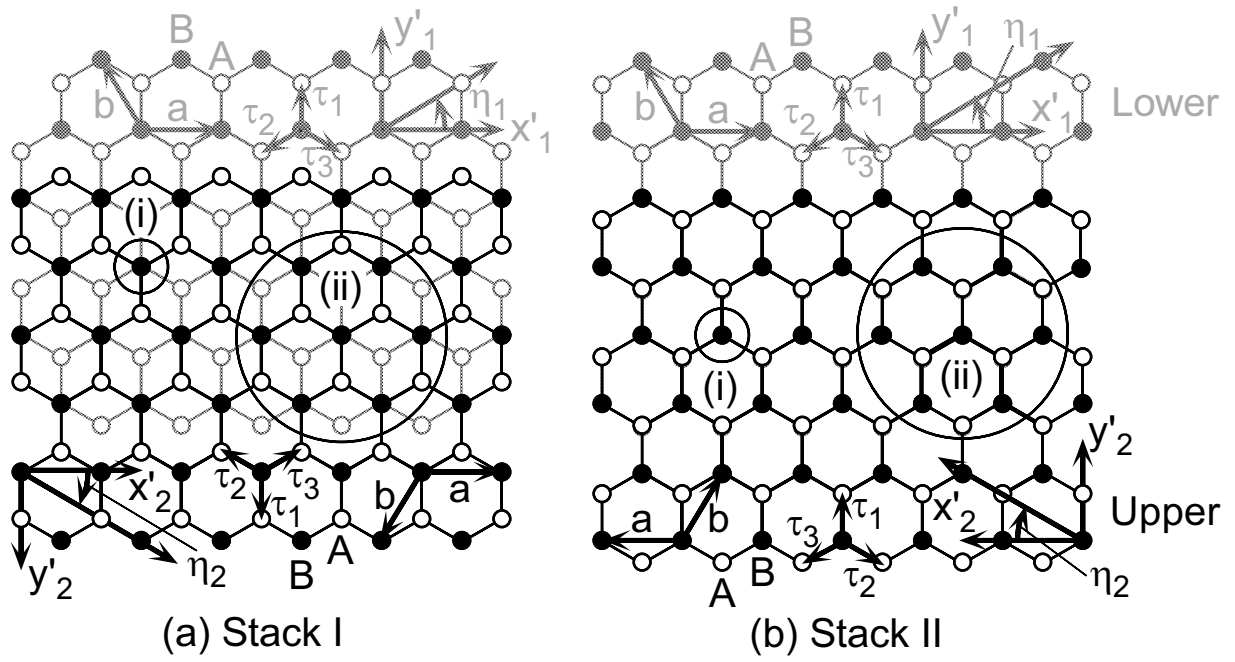


Fig. 2

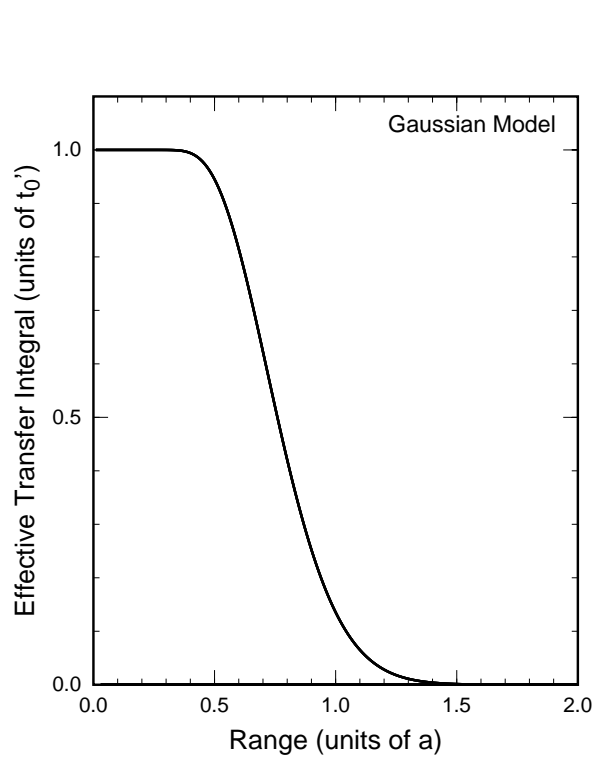


Fig. 3

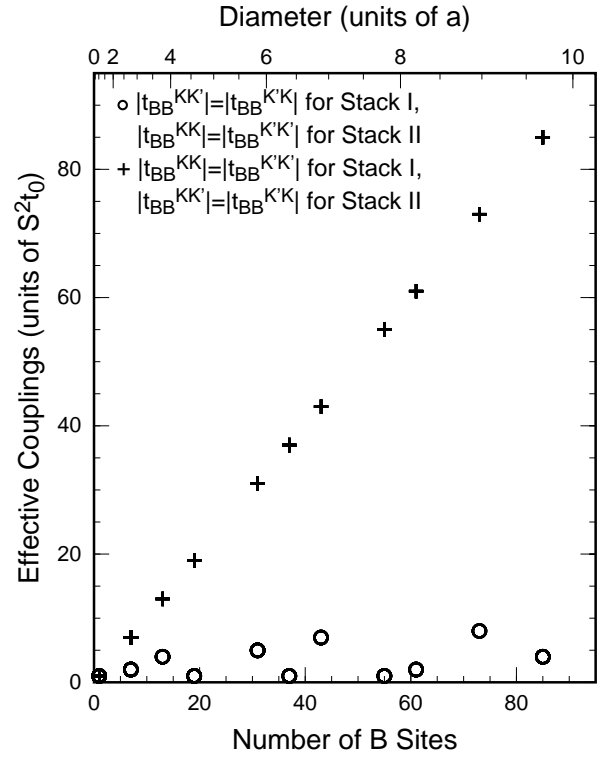


Fig. 4

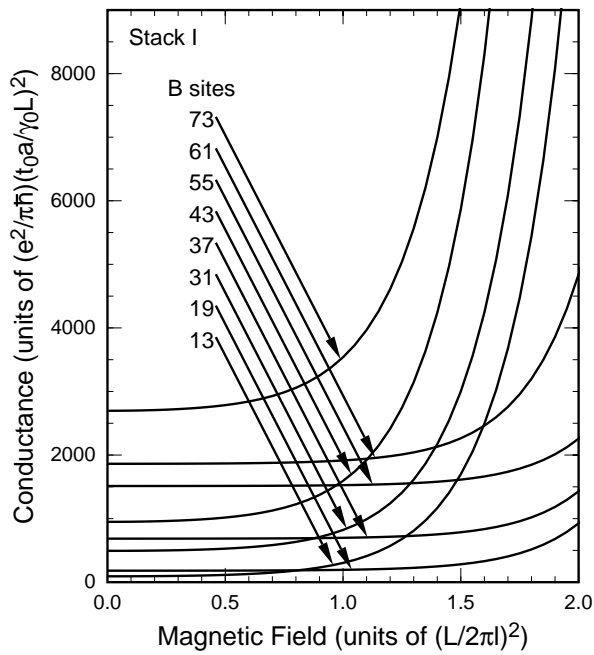


Fig. 5

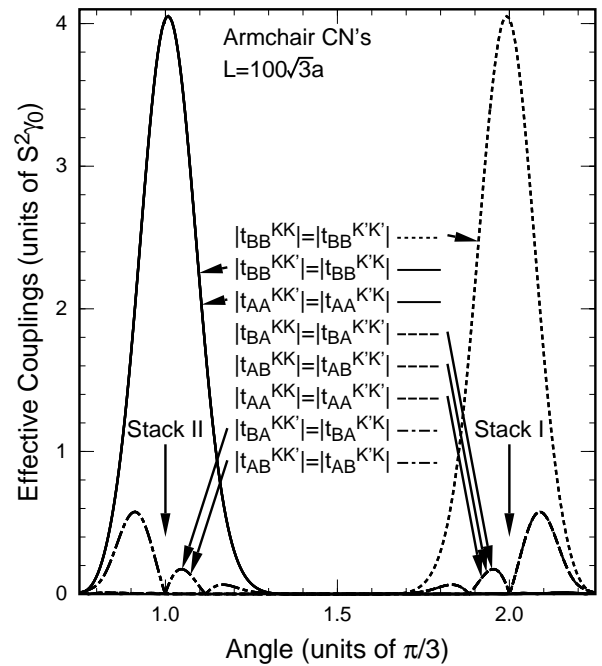


Fig. 6

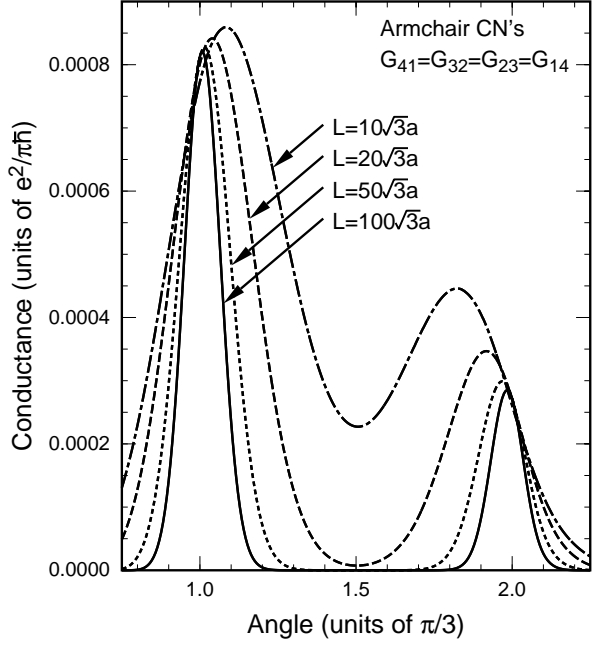


Fig. 7 (a)

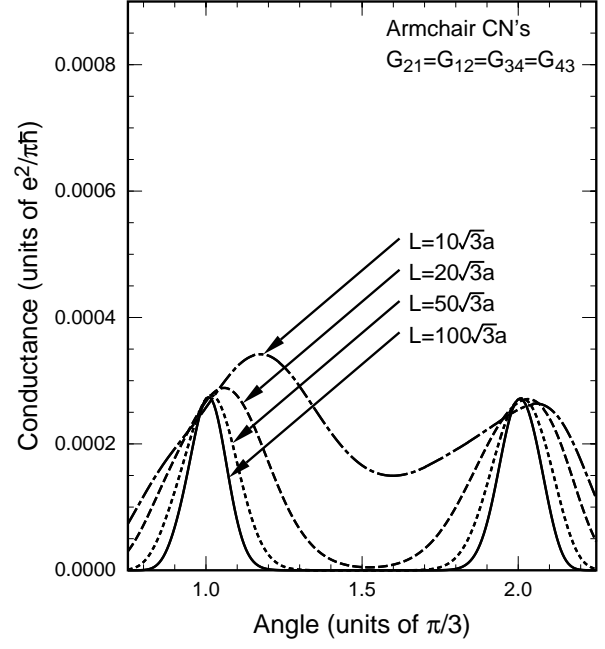


Fig. 7 (b)

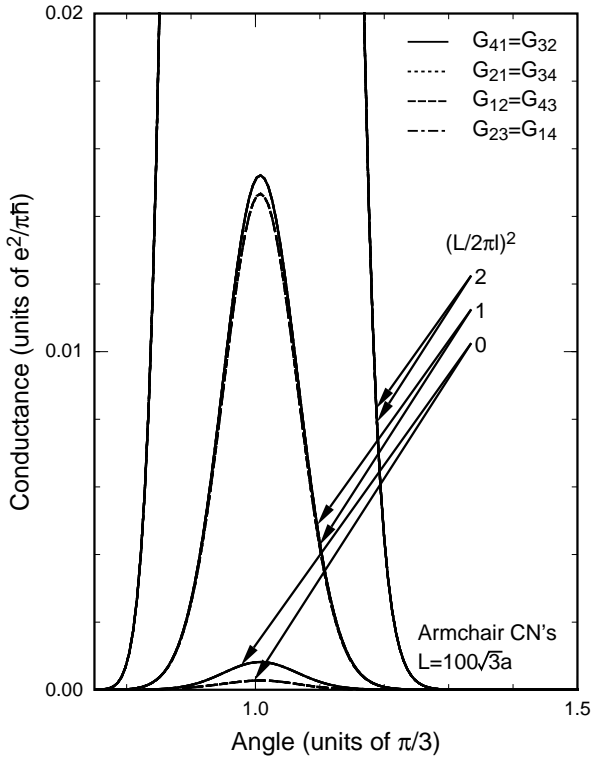


Fig. 8 (a)

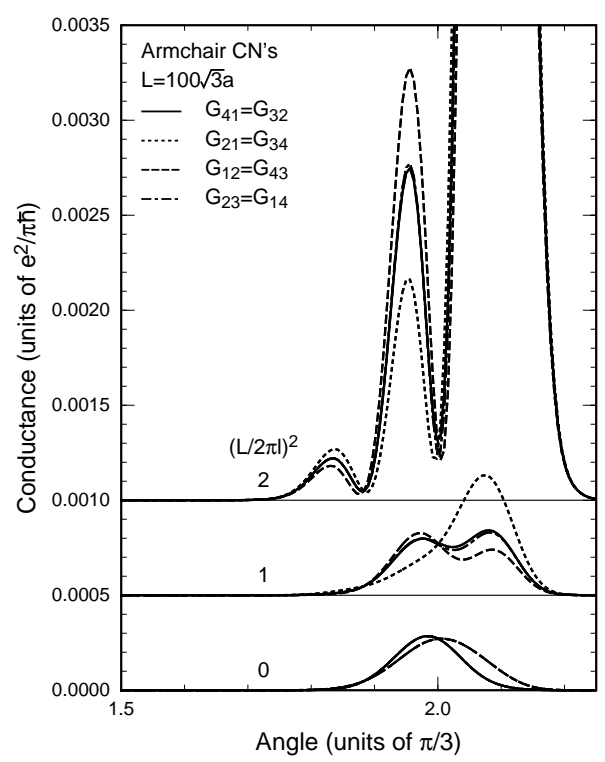


Fig. 8 (b)